Dawn-dusk asymmetry in the main auroral emissions at Jupiter observed with Juno-UVS

A. Groulard[1], B. Bonfond[1*], D. Grodent[1], J.-C. Gérard[1], T. K. Greathouse[2], V. Hue[3], G. R. Gladstone[2], M. H. Versteeg[2]

[*]Corresponding author: b.bonfond@uliege.be

[1]Laboratory for Planetary and Atmospheric Physics, Space Sciences, Technologies and Astrophysical Research Institute, University of Liège, Liège, Belgium

[2]Southwest Research Institute, San Antonio, TX, USA

[3]Aix-Marseille Université, CNRS, CNES, Institut Origines, LAM, Marseille, France

0| Abstract

Jupiter's main auroral emissions usually form auroral curtains surrounding the magnetic poles. Most explanations for this auroral feature are based on corotation enforcement currents flowing between the magnetosphere and the ionosphere. This process predicts the highest emitted power to originate from the dawn region, while the lowest emitted power would come from the noon to dusk region. However, a previous study using Hubble Space Telescope data showed the opposite, with a higher emitted power in the dusk region in the south and ambiguous results in the north. In the present study, we use data from the first 39 Juno perijoves to reexamine this question. We find a dusk region 3.3 to 5.5 times more powerful than the dawn one, in qualitative agreement with the previous study but contrary to theoretical expectations. These results support the idea that the main emissions cannot be fully described by corotation enforcement currents.

1| Introduction

The UV aurorae at Jupiter are made of various structures having different origins (see e.g. the review in Grodent, 2015). The main emissions are the most easily identifiable of them. They generally take the shape of an almost closed curtain centered on the jovimagnetic poles (the intersections of the magnetic dipole axis with the surface), with a systematic brightness decrease between 10:00 and 12:00 magnetic local time (Radioti et al., 2008). In the southern hemisphere, the nearly dipolar field gives an oval shape to the main emissions, while a magnetic anomaly related to the high order terms of the magnetic field multipolar development gives them a bean shape in the northern hemisphere (Grodent et al., 2008; Connerney et al., 2022). The persistence of this main component of the aurorae is presumably due to its formation mechanism.

The most widely accepted explanation for the main auroral emissions at Jupiter before the Juno era was related to the magnetosphere-ionosphere coupling current system enforcing the partial corotation of the plasma in the Jovian middle magnetosphere (Cowley and Bunce, 2001; Hill, 2001). When particles produced by the volcanically active moon Io are ionized, they end up forming a plasma torus around Jupiter, corotating with the planet along the moon's orbit. Because of a balance between centrifugal, thermal and Lorentz forces, the plasma in the torus progressively diffuses radially outward into a plasmasheet. A corotation enforcement current loop arises to maintain the corotation of the plasma, transferring angular momentum from Jupiter's polar atmosphere to the magnetosphere. In the equatorial plane of the magnetosphere, this current flows radially, which manifests as an azimuthal

bendback of the magnetic field lines. It then flows along magnetic field lines and closes in the ionosphere via Pedersen currents. As the iogenic plasma moves further away from the planet, the upward (relative to Jupiter) field aligned currents (FACs) enforce a significant degree of corotation (~75-90% of full corotation) up to around 20-40 R_J before the plasma's angular velocity starts to drop significantly at larger distances. The field aligned currents peak in this transition region where the corotation breaks down. According to this family of models, such upward FACs accelerate electrons towards Jupiter's atmosphere via quasi-static electric fields, generating the main auroral emissions at the feet of the field lines. The main emissions magnetically map to distances between 15 and 60 Jupiter radii (R_J) in the magnetosphere (Vogt et al., 2011), similarly to estimated magnetospheric roots of the field aligned current sheets observed by Juno (Kamran et al., 2022). This theory provides a straightforward explanation for the persistence of the main emissions over long timescales and for the existence of the field aligned currents inferred from magnetic field measurements (Kamran et al., 2022; Kotsiaros et al., 2019; Nichols and Cowley, 2022; Sulaiman et al., 2022). However, Bonfond et al., (2020) have questioned this simplified picture recently after highlighting an increasing number of observations which appear in contradiction with the model's expectations. For example, as the magnetic field topology and plasma flow are not uniform around the planet, Ray et al. (2014**)** used a 1-D model based on this theory to predict how the intensity of the main emission varies over local times. According to this model, the strongest aurorae should take place at dawn and should be at least one order of magnitude stronger than in the dusk region. . This prediction has been tested by Bonfond et al. (2015) , who used Hubble Space Telescope (HST) data to determine and compare the power emitted in the dusk and dawn parts of the main emissions. They found a dusk region about 3 times more powerful than the dawn one in the southern hemisphere, which is in disagreement with the Ray et al.

(2014) model. They also have found that both regions were equally powerful in the northern hemisphere. However, they noted that the later results should be considered with caution. Indeed, the HST observations are hampered by the telescope's viewing geometry, which is such that HST cannot observe the night side aurora and most images are acquired when the jovimagnetic pole of interest is tilted towards the Earth. This issue is more prominent in the north since the barycenter of the main auroral emission is located at lower latitude. This limitation is further magnified by the presence of a large magnetic anomaly near 100° System III longitude. System III is the longitude system fixed with Jupiter's magnetic field extensively used to study the magnetic phenomena taking place at Jupiter. Based on their results in the southern hemisphere, which they considered more reliable, the authors concluded that the main emissions cannot be fully described by the theory of partial corotation enforcement in the middle magnetosphere. The partial ring current observed at Jupiter (Khurana, 2001) has been suggested to generate FACs increasing the emitted power in the dusk region, and lowering it in the dawn region, to explain the disagreement between their results and the model. The purpose of the present study is to further constrain the findings of Bonfond et al. (2015) with observations unaffected by Earth orbit viewing geometry.

The morphology and intensity of the main emissions may also vary over a few hours. For example, instead of a simple and well defined arc, the main emissions sometimes appear to form forks and parallel arcs, and patchy features can be seen from time to time (Nichols et al., 2009). In addition to these disturbances, two kinds of events can increase the emitted power of the aurorae (Yao et al., 2022): dawn storms and main auroral brightenings. Bonfond et al. (2021) have found dawn storms in about half of the first 20 Juno perijoves (PJ). They

also extended the definition of these storms to a chain of events lasting from 5 to 10 hours, ending with 1 to 2 hours of intense brightening of the dawn region of the main emissions. A more global brightening coupled with a shrinking of the main emission can also occur during solar wind compressions of the magnetosphere (Nichols et al., 2007, 2009, 2017; Yao et al., 2022).

The discrepancy between the dawn/dusk auroral power ratio in the northern and southern hemispheres based on the HST data called for a re-investigation of this problem with unbiased data. Here we carry out a similar study, based on UV auroral observations carried out with the Ultraviolet Spectrograph on board the Juno spacecraft.

2| Observations

The NASA Juno spacecraft arrived at Jupiter on July 5th, 2016 (Bolton et al., 2017). It was placed in a highly eccentric polar orbit bringing it to an altitude of only 4000 km at its periapsis, and out to 8 million km near apoapsis well out into the magnetosphere. This orbit offers the advantage of gathering high resolution data of Jupiter, while being able to study the whole environment of the planet. Juno is a spinning spacecraft, undergoing one rotation every 30 s. It carries 10 scientific instruments, including a longslit UltraViolet Spectrograph (UVS) used in this study. UVS is a photon-counting imaging spectrograph operating in the 68-210 nm range (Gladstone et al., 2017). The UVS field of view consists of a 7.2° long slit divided into three parts. The 2 external parts are 0.2° wide, while the central one is narrower and has a width of only 0.025°. Individual photons are counted and calibrated using the effective area derived

from many stellar observations (Hue et al., 2019), while the wavelength registration comes from pre-launch measurements (Davis et al., 2011; Hue et al., 2021). As they provide a higher signal-to-noise ratio, only the external wider parts of the slit were used in this study. The data used for this study are selected among the observations acquired with Juno-UVS during four hours in each hemisphere when the spacecraft flies over the poles close to its perijove.

We first created polar brightness maps of the aurorae in the same way as described by Bonfond et al. (2021). Specifically, after removing the noise from the images, data gathered over 100 spins of the spacecraft were added and weighted to build the final map. This method has the advantage of allowing the creation of comprehensive maps of the aurorae for most of the perijoves, but the tradeoff is a long (~50 minutes) time interval between the first and the last spins. This process was repeated for the first 39 perijoves of Juno in both hemispheres. Because of the limited coverage of the poles by Juno during some perijoves, only 63 maps were considered in the study. More precisely, out of the 39 possible maps for each perijove, 38 were kept in the southern hemisphere and 25 in the northern hemisphere. The detailed times of observation for each perijove can be found in the supplementary material. In this study, we only considered the time intervals during which the high voltage was nominal. The indicated brightness is the total FUV brightness emitted by H_2 in kR units. In order to mitigate the effect of hydrocarbon absorption (especially methane, below 140 nm), we first only considered the unabsorbed 145-165 nm wavelength range and then multiplied it by a factor of 4.4 to extend the brightness to the whole FUV H_2 spectrum. To account for the fact that the assumed emitting surface is not perpendicular to the viewing axis, we multiplied the observed brightness by the cosine of the local emission angle, which typically lies around ~30-

40°. To derive the emitted power, we multiply the brightness by the mean photon energy ($1.65*10^{-18}$ J) and by the emission surface in the region of interest.

3| Analysis

While the main emissions clearly stand out when co-adding many UV auroral images, identifying them on individual images can become tricky when the morphology becomes complex (parallel arc, dawn storms, etc.). In order to get robust results, we decided to use 3 different methods to build masks isolating the main emissions and we used 2 different definitions of the dawn and dusk sectors. First, since the size of the main auroral oval varies with time, we used a pair of "generic" masks, one for a contracted auroral oval and one for an expanded auroral oval, using the one most appropriate for the case under study. This method is somewhat similar to the one used by Bonfond et al. (2015), who used monthly averaged reference ovals to build masks and then used this mask for all images during that month. Then we built "adjusted" masks, fitting the location of the main emissions as closely as possible for each individual image, but with a constant width. We then built masks by fitting both the location and the width.

3.1| Main emissions masks

The first mask built to isolate the main emissions, the Magnetospheric Distance mask (MD mask), was created based on the Vogt et al. (2011) magnetic mapping model. It is thought to

be more reliable than models based on the combination of an internal field and a current disk in the middle magnetosphere, which is the region where the plasma that feeds the main emissions is located. Indeed, it accounts for the influence of local time on the magnetic field and it is rooted on measurements of the Ganymede footprint path from the Hubble Space Telescope and of magnetic flux in the equatorial plane from Galileo. Using this model, two masks were created to cover locations mapping to a constant distance of 30 and 40 R_J in the magnetosphere to take into account the variable location of the main emissions. Indeed, as already mentioned, Vogt et al. (2011) have found the main emission to map between 15 and 60 R_J in the magnetosphere. We chose distances of 30 and 40 R_J as it is in the middle of this interval so that we have better chances of covering the main emissions well. To do so, we chose 36 equally spaced local times. Those are used to find the longitude and latitude of the ionospheric locations mapping to these local times at a distance of 30 and 40 R_J in the magnetosphere based on the Vogt et al. (2011) model. These ionospheric locations have then been interpolated to obtain ribbons covering all longitudes. At each point constituting the ribbons, the widths of the ribbons have then been extended to 2° in the direction of the axis linking that point to the barycenter of the aurorae, so that the masks overlap most of the main auroral emissions without including contributions from other auroral features. As the main emissions morphology changes over time, the location of its barycenter can also slightly move. Still, in this study we assumed the barycenter to be located at 73.9° latitude and 185.6° System III longitude in the north; and -81.9° latitude and 31.9° System III longitude in the south since its exact location does not have a marked impact on our results. These locations have been derived from images coming from the 2007 HST campaign. To choose between the contracted oval mask and the expanded oval mask, we computed the total power in the area covered by both masks. The mask with the largest total power was kept as the MD mask

(Figure 1, panel 2a), while the other one was discarded. In order to be able to select sub-elements of this mask corresponding to the different local time sectors, our masks are not just binary masks, but each element of the mask is attributed a value related to the angle centered on the barycenter of the aurorae (Figure 1, panel 2b).

The two other masks were created based on the actual location of the MEs in the images. Because arcs can be present not only in the MEs, but also on the polar region and in the equatorward emissions, we must exclude these regions from our search and focus on the region where they are the most likely to appear. To do so, we decided to use as a first guess the suite of masks based on the 2007 HST campaign (Bonfond et al., 2012; Clarke et al., 2009)The HST mask with the best overlap of the main emission was chosen as a starting point. For each tenth of a degree of longitude, the brightness peak was searched in the surrounding of the HST mask, assuming this peak is due to the main emissions. The HST mask has essentially been used to restrict the search area and make sure to discard the IFP which can be brighter than the main emissions in some locations. For areas where the main emissions are fainter than usual, the highest gradient of brightness was searched instead of the highest brightness. Indeed, based on the idea that the main emissions are associated with FACs due to corotation enforcement, they should correspond to an auroral curtain with a higher peak brightness than its surrounding, and a high gradient of brightness should be present at its edges. Once done for all the longitudes of interest, a Fourier series was fitted to the locations thus found. This method results in a smooth ribbon at the center of the main emissions. As for the MD mask, the ribbon was extended to be 2° wide to cover the whole width of the main emissions. An example of such an AF1 mask over the aurorae can be seen in Figure 1, panel

3a. The mask also has different values for different angles around the barycenter of the aurorae for later considerations (Figure 1, panel 3b).

The last mask is the Auroral Fit with variable width mask (AF2 mask). It has been created to take into account the complex shape that the main emissions can take during some perijoves. When the main emissions are composed of parallel arcs or unusual particularly wide features, it can be more extended than 2°. Thus, the two first masks may be too narrow in several places, and a third one is needed to more accurately deal with these unusual cases. To create the AF2 mask, we started from the boundaries of the AF1 mask. To find broad auroral main emissions, we looked for high brightness regions partly covered by the AF1 mask. To do so, we used a brightness threshold defined based on the brightness of the area covered by the AF1 mask for each tenth of degree around the barycenter. If there are emissions above that threshold just outside the AF1 mask, they are considered as part of the main emissions and they must be covered by the mask. In this case, new limits are defined to encompass them. If there is no such bright region, the AF1 limits are kept. After that, the new inner and outer limits have been fitted independently with Fourier series, so that it gives two ribbons that serve as the limits of the AF2 mask. This way, the mask is at least 2° wide in latitude, but can be broader if the main emissions are more extended at some locations (Figure 1, panel 4a). As for the two other masks, the value of the different points of the mask is linked to its angle around the barycenter of the aurorae (Figure 1, panel 4b). This mask is a generalized version of the AF1 mask. It has been needed for 27 of the 63 maps, since its usefulness relies on an unusual shape of the main emissions. Out of them, 8 are in the northern hemisphere, and 19

in the southern one. Even for these maps, the broadening of the mask is not necessarily in the dusk or dawn region, and the AF2 mask only has an impact on few perijoves.

3.2| Dawn and dusk regions selection

Two different local time extents of the dusk and dawn regions in the magnetosphere were selected to study the emitted power. The first one, the B15 sector, ranges from 16:00 to 18:00 LT in the dusk region, and from 06:00 to 08:00 LT in the dawn region. Its size was set to match the study performed by Bonfond et al. (2015) in order to compare our results to theirs. The second one, the SYM sector, ranges from 16:00 LT to 20:00 LT in the dusk region, and from 04:00 LT to 08:00 LT in the dawn one. This sector is symmetrical over the dusk local time (i.e.: 18:00 LT) and the dawn local time (i.e.: 06:00 LT), which is a more natural choice to study these regions. This sector could not be studied with HST due to its orbit that did not allow for a view of the night part of the planet.

We used the Vogt et al. (2011) magnetic mapping model, with the JRM09 model (Connerney et al., 2018) as input magnetic field model, to link the desired local times in the magnetosphere to locations in the ionosphere. Each magnetospheric local time corresponds to a given angle relative to the barycenter of the aurorae in the ionosphere. The model provides a longitude-latitude location in the ionosphere from a location with a known longitude and distance in the magnetosphere. The desired local times are used as the input longitude, and a distance of 30 R_J is used as the input distance since it is expected to map to

the main emissions. All the ionospheric longitude-latitude coordinates can then be transformed into polar coordinates. Thanks to the way the three masks were created, with the value of a location proportional to its angle around the barycenter (Figures 1, panels b), one can easily find the different sectors in the ionosphere from the locations expressed in polar coordinates. This way, we have limited the main emissions masks to the two sectors of interest to study the emitted power from the two regions.

The maps that could not be used at all because the aurorae were not well imaged have already been ruled out of the study, but additional problems arise. Some UVS auroral maps are incomplete in a part of the dusk or dawn region, and the main emissions mask is not accurately placed in others. The second case mostly happens for the MD mask, which maps to a constant distance in the magnetosphere, while the origin of the main emissions is at a variable distance (see the example of PJ12 north in the supplemental material). Bonfond et al. (2015) had already noted that in some rare cases, their generic monthly oval would completely miss the aurora on one side (generally the dusk one). Because these cases are both rare and lead to obviously erroneous results, the study has been restricted to 338 sectors out of the 378 possible sectors of the 63 maps.

4| Results and discussion

For each sector, the dusk-over-dawn power ratio was computed, and the results can be seen in Figure 2. In the dataset of UVS auroral images analyzed here, the dusk sector is brighter than the dawn sector in ~85% of the cases. Regardless of the size of the sector, the reference

oval in use and the assumed auroral width, the median power ratios are several times larger than unity, indicating a dusk region more powerful than the dawn one (Table 1). We note that, compared to a "generic mask" such as our MS mask, adjusting for the precise location of the main emissions (AF1 masks), and to their width (AF2 masks) tends to increase the value of the median ratio. This is because the adjusted masks better select the more variable dusk arc (or multiple arcs). Furthermore, we note that, while the AF2 masks, being wider, may capture emissions arising from different mechanisms than the rest of the MEs, the inclusion of a larger region does not fundamentally modify the results.

In the B15 sector, the median ratio varies from 3.4 (MD mask) to 3.9 (AF2 mask) in the northern hemisphere, while in the southern hemisphere it varies from 4.2 (MD mask) to 5.5 (AF2 mask). Thus, our results are qualitatively similar to those obtained by Bonfond et al., 2015 in the south (a median dusk/dawn ratio of 3.1).. Additionally, our values in the north are relatively similar to those in the south (3.4 compared to 4.2 for the B15 sector and the MD mask, which the combination closest to the method used in Bonfond et al. 2015). This result validates the reservations of Bonfond et al. (2015) concerning their own results in north, which they considered unreliable because they were tainted by a selection bias. Nevertheless, we note that our value in the south remains higher than the one deduced from the HST images. We attribute at least part of the difference in the results to the color ratio (CR) assumed to be constant over the main emissions in the previous study. The color ratio measures the absorption of light from the atmospheric constituents and is given by the ratio of intensity of light in an unabsorbed band (155-162 nm) and the intensity in an absorbed band (123-130 nm) (Yung et al., 1982; Gustin et al., 2012). By assuming a constant CR, they considered all the emissions to take place at the same depth. Gérard et al. (2016) have shown that the brightness and the color ratio are correlated in the main emissions. The throughput

of the broadband filter used for Far-UV imaging with the Space Telescope Imaging Spectrograph (STIS) and the Advanced Camera for Surveys (ACS) have a triangular shape (see Figure1 in Gustin et al. 2012), putting an emphasis on the shorter wavelengths (those absorbed by methane) Hence, for a similar initial brightness, the more absorbed emissions appear attenuated in the images. As a consequence, when the color ratio and brightness are correlated, the apparent contrast between bright and absorbed features on one hand and dim but less absorbed features on the other hand is reduced. Because the Juno-UVS observations provide spectral information between 68-210 nm, it is possible to multiply the observed spectra by the throughput of the filters used by the cameras on board HST to simulate these observations. A test applied to the southern hemisphere during PJ4 indeed showed that the use of the throughput of the HST SrF2 filter led to a ~10% decrease on the dusk/dawn ratio, compared to the unaltered UVS brightness. However, this computation assumes that HST can observe the Jovian pole from the same vantage point as Juno. Changing the elevation angle from ~30° to ~80° would further increase the CR contrast and thus decrease the dusk/dawn ratio.

Slightly lower dusk-over-dawn ratios are found in the SYM sector, with median ratios on the order of 2.9 to 4.0. We attribute this to the size of the sectors. Indeed, the SYM sector is twice larger than the B15. Thus, there are more chances for a bright patch of emission to be covered by a given mask in the SYM sector. If this patch is in the dusk region, it has a low impact on the ratio since the dusk region is generally made of bright emissions. Conversely, if the patch is in the dawn region, it can have a larger impact, which results in lowering the power ratio. Either way, we found a brighter dusk region for both sectors.

We computed the mean value and the variance of the emitted power in the different sectors (table S4) and we did not find that the variance is significant different in one sector compared to the other. Thus, the variability of the ratio cannot be preferentially attributed to one local time sector. The power difference between the dusk and dawn sectors could have been used as an alternative parameter (see its median values in table S3), but it would lead to the same general conclusion, with the drawback of being sensitive to the size of the sectors.

Some perijoves displayed a more powerful dawn region. This is the case for PJ3, 10, 12, 15, 18, 26 and 32. Different reasons can explain this trend. First, we have found dawn storms during PJ3 and PJ32. These are not the only perijoves during which dawn storms have been observed, but the others are captured at stages where the power amplification is not yet present or significant enough to inverse the ratio. During PJ10, 12, 15 and 18, a main aurora brightening (MAB) and a compression of the main emissions are visible. This case is often coupled with a more complex morphology of the main emissions in the dusk region. Such auroral morphologies are generally associated with the arrival of a solar wind shock (Grodent et al., 2018; Nichols et al., 2007; Yao et al., 2022). Therefore, the MD and AF1 masks cannot cover the whole main emissions, and the dawn region seems more powerful with these masks. When using the AF2 mask, the dusk region can be better covered, and the power ratio goes back to a value closer to unity. No trend can be identified concerning the more powerful region in this case, as the ratios have values slightly higher or lower than unity. In the case of PJ26, the main emissions vanished in the dusk region of the northern hemisphere, which led to the dawn section being brighter than the dusk one. The three explanations for these low ratios are illustrated in Figure 3.

5| Summary and conclusion

Using data gathered over the first 39 Juno perijoves, we have conducted a study of the emitted power from the dusk and dawn regions of the main emissions. To analyze the impact of the accuracy of the identification of the main emissions on the results, 3 different masks have been created to isolate the regions. The first one uses the Vogt et al. (2011) model to link the magnetospheric plasma to auroral features in order to build a "generic" mask. The second one is built specifically for each image and covers the region of highest brightness, assuming it is the main emissions. Finally, the third one is similar to the second one, but with a variable width permitted to cover the wider parts of the main emissions. In addition to these 3 masks, 2 sectors have been chosen for the study. The first sector extends from 16:00 to 18:00 LT in the dusk region, and from 06:00 to 08:00 LT in the dawn one, allowing for comparisons with previous results from Bonfond et al. (2015). The second sector range chosen is an extension of the first one to set it symmetrically with respect to the 18:00 LT and 06:00 LT directions, i.e., 16:00 to 20:00 LT in the dusk region, and 04:00 to 08:00 LT in the dawn region. Our analyses show that, whatever the combination of mask and sector, we obtain the same results:

- The median dusk-over-dawn power ratios are ~3-4 times higher than unity for every hemisphere, mask and sector, indicative of a dusk region generally more powerful. We

note that this behavior is seen whether the dusk-side main emissions are formed of a single regular arc (e.g. PJ8 south) or display a more complex morphology.

- Some perijoves displayed a dawn region more powerful than the dusk one, and 3 main reasons can be evoked to explain it. There have been dawn storms during some perijoves, main auroral brightenings due to increases in the solar wind ram pressure in some others, and a surprising disappearance of the main emissions in the dusk region has been found in the northern hemisphere of PJ26.

Our results are similar to those obtained by Bonfond et al. (2015) in the southern hemisphere and are still opposite to the expectations from the modeling of (Ray et al., 2014). The former suggested that, if the main emissions brightness is proportional to the field aligned currents in the middle magnetosphere, then this asymmetry could be qualitatively compatible with the combination of the upward (relative to the ionosphere) FACs related to the corotation breakdown in the middle magnetosphere and the FACs closing the partial ring currents in the ionosphere flowing downward in the dawn sector and upward in the dusk sector (aka. Region 2 currents). Lorch et al. (2020) used data gathered over 39 years with 7 spacecraft to study the asymmetry in the magnetodisk currents. They found that azimuthal currents are fed at dusk and removed at dawn, in agreement with the concept of partial ring current, confirming earlier results from Khurana (2001). On the other hand, they also showed that the radial currents were weaker on the dusk side compared to the dawn side beyond $30R_J$. Thus, because they arise from the combination of these opposite effects, the inferred total field aligned currents do not bear a clear and unambiguous imprint of region 2 currents able to explain the auroral observations discussed here. (Nichols and Cowley, 2022) showed an

391 excellent temporal correlation between the radial currents and the auroral brightness of the
392 MEs on the dawn side. They also concluded that the FACs related to the closure of the partial
393 ring current in the dawn sector should be ~10 times smaller than those associated with the
394 drop of corotation in the middle magnetosphere (0.25 $\mu A/m^2$ compared to 1-3 $\mu A/m^2$) and
395 thus have a limited influence on the aurora. Since the dusk side has the weakest radial
396 currents but the brightest auroral emissions, we must conclude that, despite the good
397 temporal correlation observed on the dawn side, there is no spatial correlation between the
398 aurora and the radial currents. Furthermore, if the closing of the partial ring current does not
399 trigger a large auroral response, then the auroral emissions do not provide a faithful image of
400 the field aligned currents, even in the MEs region. An alternative or supplemental explanation
401 for the main emissions could arise from the finding of stronger plasma turbulences on the
402 dusk side of the magnetosphere below 50 RJ compared to the dawn side (Tao et al., 2015).
403 Indeed, other aurora triggering processes involving ultra-low frequency (ULF) waves and/or
404 Alfvén waves have been discussed (Nichols et al., 2017b; Saur et al., 2018; Pan et al., 2021;
405 Lorch et al., 2022; Feng et al., 2022) and their impact on the brightness and morphology of
406 the UV auroral emissions would certainly deserve a closer exploration in a near future as the
407 evolution of Juno's orbit now allows dawn/dusk comparisons.

408

409

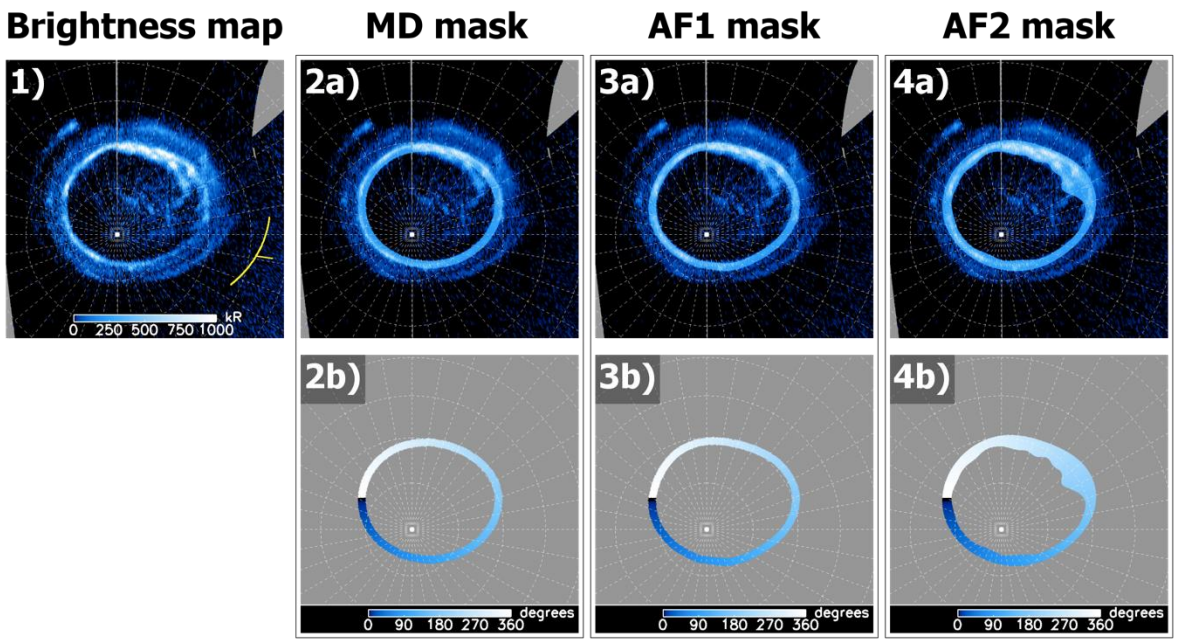

410

411 Figure 1: 1) Polar projection of the southern pole during PJ38. The sunward directions spanned over
412 the data used to create the map are indicated by a yellow region, with the radially extended part
413 referring to the mean sunward direction that has been used for the computations. For panels 2, 3 and
414 4, images a) are the same polar projection as panel 1 with MD, AF1 and AF2 masks respectively added
415 on. Images b) are polar projections of the masks alone.

416

417

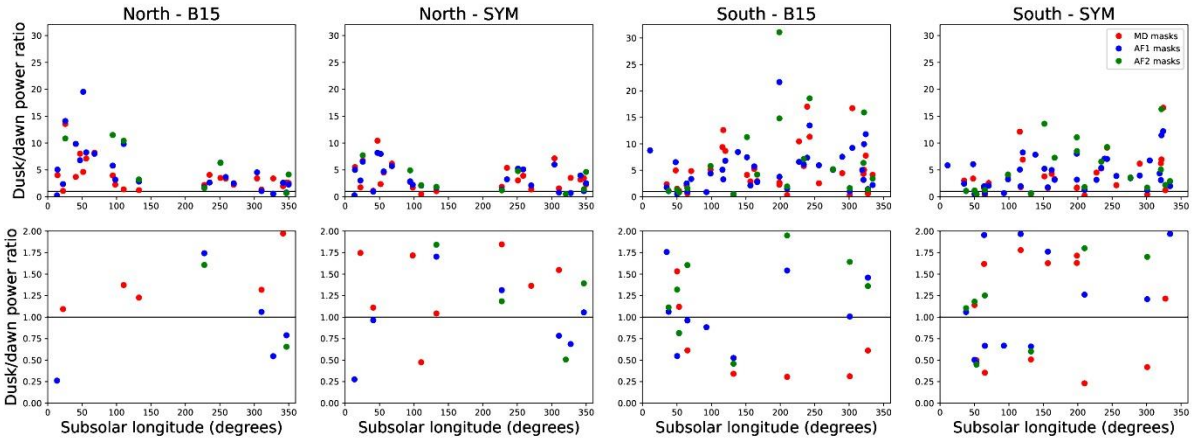

418

419 Figure 2: Top: dusk-over-dawn power ratios for the different sectors as a function of subsolar
420 longitude. Bottom: Zoomed version of the same plot, centered on the value 1. One can see that the
421 different methods can provide different results for individual cases, but for every method, dusk-over-
422 dawn ratios above 1 vastly outnumber those under 1.

423

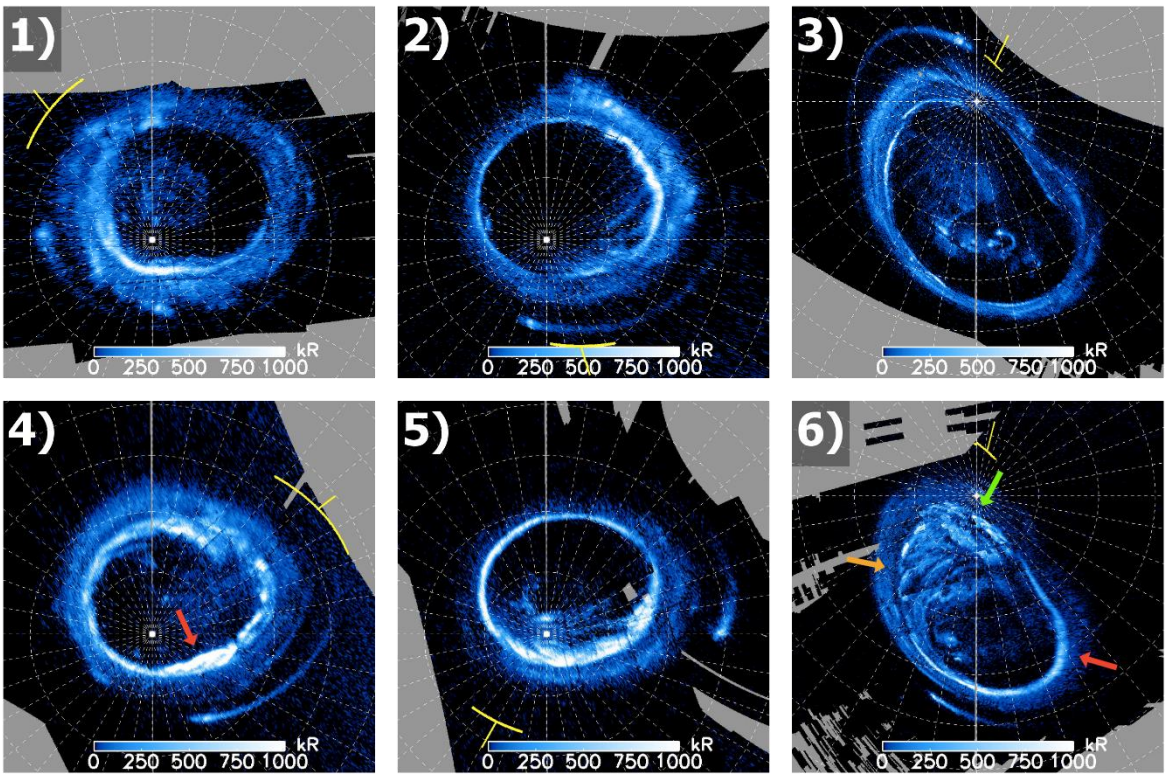

Figure 3: Illustration of three typical cases where the dusk region is more powerful than the dawn one (top line) and three atypical cases where the dawn region is more powerful than the dusk one (bottom line). The yellow arc and tick mark show the orientation of the Sun during the image acquisition. 1) Polar projection of the southern pole during PJ5. 2) Polar projection of the southern pole during PJ7. 3) Polar projection of the northern pole during PJ13. 4) Polar projection of the southern pole during PJ32. A dawn storm is indicated by the red arrow. 5) Polar projection of the southern pole during PJ12. An enhancement of the main emissions at all longitudes is visible. 6) Polar projection of the northern pole during PJ26. The red arrow points toward the dawn part of the main emissions where they are clearly visible. The green arrow points toward the noon part, where they are harder to distinguish from the polar emissions but still recognizable. Finally, the orange arrow points toward the dusk region, where the main emissions vanished and a strong decrease in the brightness is visible between the polar and outer emissions. In the three images, the sunward direction is indicated the same way as in Figure 1.

		B15 sector Median	SYM sector Median
MD mask	North	3.40	3.04
	South	4.24	2.92
AF1 mask	North	3.43	2.94
	South	4.73	3.22
AF2 mask	North	3.91	3.25
	South	5.47	4.04

Table 1: Median dusk-over-dawn power ratios for the MD, AF1 and AF2 masks in the southern and northern hemispheres, for both the B15 and SYM sectors.

6| Acknowledgements

We are grateful to NASA and contributing institutions which have made the Juno mission possible. B. Bonfond is a Research Associate of the Fonds de la Recherche Scientifique - FNRS. B. Bonfond, D. Grodent and J.-C. Gérard acknowledge financial support from the Belgian Federal Science Policy Office (BELSPO) via the PRODEX Programme of ESA. This work was funded by NASA's New Frontiers Program for Juno via contract with the Southwest Research Institute. VH acknowledges support from the French government under the France 2030 investment plan, as part of the Initiative d'Excellence d'Aix-Marseille Université – A*MIDEX AMX-22-CPJ-04.

References

Bolton, S.J., Lunine, J., Stevenson, D., Connerney, J.E.P., Levin, S., Owen, T.C., Bagenal, F., Gautier, D., Ingersoll, A.P., Orton, G.S., Guillot, T., Hubbard, W., Bloxham, J., Coradini, A., Stephens, S.K., Mokashi, P., Thorne, R., Thorpe, R., 2017. The Juno Mission. Space Sci Rev 213, 5–37. https://doi.org/10.1007/s11214-017-0429-6

Bonfond, B., Grodent, D., Gérard, J.-C., Stallard, T., Clarke, J.T., Yoneda, M., Radioti, A., Gustin, J., 2012. Auroral evidence of Io's control over the magnetosphere of Jupiter. Geophysical Research Letters 39. https://doi.org/10.1029/2011GL050253

Bonfond, B., Gustin, J., Gérard, J.-C., Grodent, D., Radioti, A., Palmaerts, B., Badman, S.V., Khurana, K.K., Tao, C., 2015. The far-ultraviolet main auroral emission at Jupiter – Part 1: Dawn–dusk brightness asymmetries. Annales Geophysicae 33, 1203–1209. https://doi.org/10.5194/angeo-33-1203-2015

Bonfond, B., Yao, Z., Grodent, D., 2020. Six Pieces of Evidence Against the Corotation Enforcement Theory to Explain the Main Aurora at Jupiter. Journal of Geophysical Research: Space Physics 125, e2020JA028152. https://doi.org/10.1029/2020JA028152

Bonfond, B., Yao, Z.H., Gladstone, G.R., Grodent, D., Gérard, J.-C., Matar, J., Palmaerts, B., Greathouse, T.K., Hue, V., Versteeg, M.H., Kammer, J.A., Giles, R.S., Tao, C., Vogt, M.F., Mura, A., Adriani, A., Mauk, B.H., Kurth, W.S., Bolton, S.J., 2021. Are Dawn Storms Jupiter's Auroral Substorms? AGU Advances 2, e2020AV000275. https://doi.org/10.1029/2020AV000275

Clarke, J.T., Nichols, J., Gérard, J.-C., Grodent, D., Hansen, K.C., Kurth, W., Gladstone, G.R., Duval, J., Wannawichian, S., Bunce, E., Cowley, S.W.H., Crary, F., Dougherty, M., Lamy, L.,

Mitchell, D., Pryor, W., Retherford, K., Stallard, T., Zieger, B., Zarka, P., Cecconi, B., 2009. Response of Jupiter's and Saturn's auroral activity to the solar wind. Journal of Geophysical Research: Space Physics 114. https://doi.org/10.1029/2008JA013694

Connerney, J.E.P., Kotsiaros, S., Oliversen, R.J., Espley, J.R., Joergensen, J.L., Joergensen, P.S., Merayo, J.M.G., Herceg, M., Bloxham, J., Moore, K.M., Bolton, S.J., Levin, S.M., 2018. A New Model of Jupiter's Magnetic Field From Juno's First Nine Orbits. Geophysical Research Letters 45, 2590–2596. https://doi.org/10.1002/2018GL077312

Connerney, J.E.P., Timmins, S., Oliversen, R.J., Espley, J.R., Joergensen, J.L., Kotsiaros, S., Joergensen, P.S., Merayo, J.M.G., Herceg, M., Bloxham, J., Moore, K.M., Mura, A., Moirano, A., Bolton, S.J., Levin, S.M., 2022. A New Model of Jupiter's Magnetic Field at the Completion of Juno's Prime Mission. Journal of Geophysical Research: Planets 127, e2021JE007055. https://doi.org/10.1029/2021JE007055

Cowley, S.W.H., Bunce, E.J., 2001. Origin of the main auroral oval in Jupiter's coupled magnetosphere–ionosphere system. Planetary and Space Science, Magnetosphere of the Outer Planets Part II 49, 1067–1088. https://doi.org/10.1016/S0032-0633(00)00167-7

Davis, M.W., Gladstone, G.R., Greathouse, T.K., Slater, D.C., Versteeg, M.H., Persson, K.B., Winters, G.S., Persyn, S.C., Eterno, J.S., 2011. Radiometric performance results of the Juno ultraviolet spectrograph (Juno-UVS), in: UV/Optical/IR Space Telescopes and Instruments: Innovative Technologies and Concepts V. Presented at the UV/Optical/IR Space Telescopes and Instruments: Innovative Technologies and Concepts V, SPIE, pp. 42–54. https://doi.org/10.1117/12.894274

Feng, E., Zhang, B., Yao, Z., Delamere, P.A., Zheng, Z., Brambles, O.J., Ye, S.-Y., Sorathia, K.A., 2022. Dynamic Jovian Magnetosphere Responses to Enhanced Solar Wind Ram Pressure: Implications for Auroral Activities. Geophysical Research Letters 49, e2022GL099858. https://doi.org/10.1029/2022GL099858

Gérard, J.-C., Bonfond, B., Grodent, D., Radioti, A., 2016. The color ratio-intensity relation in the Jovian aurora: Hubble observations of auroral components. Planetary and Space Science 131, 14–23. https://doi.org/10.1016/j.pss.2016.06.004

Gladstone, G.R., Persyn, S.C., Eterno, J.S., Walther, B.C., Slater, D.C., Davis, M.W., Versteeg, M.H., Persson, K.B., Young, M.K., Dirks, G.J., Sawka, A.O., Tumlinson, J., Sykes, H., Beshears, J., Rhoad, C.L., Cravens, J.P., Winters, G.S., Klar, R.A., Lockhart, W., Piepgrass, B.M., Greathouse, T.K., Trantham, B.J., Wilcox, P.M., Jackson, M.W., Siegmund, O.H.W., Vallerga, J.V., Raffanti, R., Martin, A., Gérard, J.-C., Grodent, D.C., Bonfond, B., Marquet, B., Denis, F., 2017. The Ultraviolet Spectrograph on NASA's Juno Mission. Space Sci Rev 213, 447–473. https://doi.org/10.1007/s11214-014-0040-z

Grodent, D., 2015. A Brief Review of Ultraviolet Auroral Emissions on Giant Planets. Space Sci Rev 187, 23–50. https://doi.org/10.1007/s11214-014-0052-8

Grodent, D., Bonfond, B., Gérard, J.-C., Radioti, A., Gustin, J., Clarke, J.T., Nichols, J., Connerney, J.E.P., 2008. Auroral evidence of a localized magnetic anomaly in Jupiter's

northern hemisphere. Journal of Geophysical Research: Space Physics 113. https://doi.org/10.1029/2008JA013185

Grodent, D., Bonfond, B., Yao, Z., Gérard, J.-C., Radioti, A., Dumont, M., Palmaerts, B., Adriani, A., Badman, S.V., Bunce, E.J., Clarke, J.T., Connerney, J.E.P., Gladstone, G.R., Greathouse, T., Kimura, T., Kurth, W.S., Mauk, B.H., McComas, D.J., Nichols, J.D., Orton, G.S., Roth, L., Saur, J., Valek, P., 2018. Jupiter's Aurora Observed With HST During Juno Orbits 3 to 7. Journal of Geophysical Research: Space Physics 123, 3299–3319. https://doi.org/10.1002/2017JA025046

Gustin, J., Bonfond, B., Grodent, D., Gérard, J.-C., 2012. Conversion from HST ACS and STIS auroral counts into brightness, precipitated power, and radiated power for H2 giant planets. Journal of Geophysical Research: Space Physics 117. https://doi.org/10.1029/2012JA017607

Hill, T.W., 2001. The Jovian auroral oval. J. Geophys. Res. 106, 8101–8108. https://doi.org/10.1029/2000JA000302

Hue, V., Giles, R.S., Gladstone, G.R., Greathouse, T.K., Davis, M.W., Kammer, J.A., Versteeg, M.H., 2021. Updated radiometric and wavelength calibration of the Juno ultraviolet spectrograph. Journal of Astronomical Telescopes, Instruments, and Systems 7, 044003. https://doi.org/10.1117/1.JATIS.7.4.044003

Hue, V., Gladstone, G.R., Greathouse, T.K., Kammer, J.A., Davis, M.W., Bonfond, B., Versteeg, M.H., Grodent, D.C., Gérard, J.-C., Bolton, S.J., Levin, S.M., Byron, B.D., 2019. In-flight Characterization and Calibration of the Juno-ultraviolet Spectrograph (Juno-UVS). The Astronomical Journal 157, 90. https://doi.org/10.3847/1538-3881/aafb36

Kamran, A., Bunce, E.J., Cowley, S.W.H., James, M.K., Nichols, J.D., Provan, G., Cao, H., Hue, V., Greathouse, T.K., Gladstone, G.R., 2022. Auroral Field-Aligned Current Signatures in Jupiter's Magnetosphere: Juno Magnetic Field Observations and Physical Modeling. Journal of Geophysical Research: Space Physics 127, e2022JA030431. https://doi.org/10.1029/2022JA030431

Khurana, K.K., 2001. Influence of solar wind on Jupiter's magnetosphere deduced from currents in the equatorial plane. Journal of Geophysical Research: Space Physics 106, 25999–26016. https://doi.org/10.1029/2000JA000352

Kotsiaros, S., Connerney, J.E.P., Clark, G., Allegrini, F., Gladstone, G.R., Kurth, W.S., Mauk, B.H., Saur, J., Bunce, E.J., Gershman, D.J., Martos, Y.M., Greathouse, T.K., Bolton, S.J., Levin, S.M., 2019. Birkeland currents in Jupiter's magnetosphere observed by the polar-orbiting Juno spacecraft. Nat Astron 3, 904–909. https://doi.org/10.1038/s41550-019-0819-7

Lorch, C.T.S., Ray, L.C., Arridge, C.S., Khurana, K.K., Martin, C.J., Bader, A., 2020. Local Time Asymmetries in Jupiter's Magnetodisc Currents. Journal of Geophysical Research: Space Physics 125, e2019JA027455. https://doi.org/10.1029/2019JA027455

Lorch, C.T.S., Ray, L.C., Wilson, R.J., Bagenal, F., Crary, F., Delamere, P.A., Damiano, P.A., Watt, C.E.J., Allegrini, F., 2022. Evidence of Alfvénic Activity in Jupiter's Mid-To-High Latitude

554 Magnetosphere. Journal of Geophysical Research: Space Physics 127, e2021JA029853.
555 https://doi.org/10.1029/2021JA029853

556 Nichols, J.D., Badman, S.V., Bagenal, F., Bolton, S.J., Bonfond, B., Bunce, E.J., Clarke, J.T.,
557 Connerney, J.E.P., Cowley, S.W.H., Ebert, R.W., Fujimoto, M., Gérard, J.-C., Gladstone, G.R.,
558 Grodent, D., Kimura, T., Kurth, W.S., Mauk, B.H., Murakami, G., McComas, D.J., Orton, G.S.,
559 Radioti, A., Stallard, T.S., Tao, C., Valek, P.W., Wilson, R.J., Yamazaki, A., Yoshikawa, I.,
560 2017a. Response of Jupiter's auroras to conditions in the interplanetary medium as
561 measured by the Hubble Space Telescope and Juno. Geophysical Research Letters 44, 7643–
562 7652. https://doi.org/10.1002/2017GL073029

563 Nichols, J.D., Bunce, E.J., Clarke, J.T., Cowley, S.W.H., Gérard, J.-C., Grodent, D., Pryor, W.R.,
564 2007. Response of Jupiter's UV auroras to interplanetary conditions as observed by the
565 Hubble Space Telescope during the Cassini flyby campaign. Journal of Geophysical Research:
566 Space Physics 112. https://doi.org/10.1029/2006JA012005

567 Nichols, J.D., Clarke, J.T., Gérard, J.C., Grodent, D., Hansen, K.C., 2009. Variation of different
568 components of Jupiter's auroral emission. Journal of Geophysical Research: Space Physics
569 114. https://doi.org/10.1029/2009JA014051

570 Nichols, J.D., Cowley, S.W.H., 2022. Relation of Jupiter's Dawnside Main Emission Intensity
571 to Magnetospheric Currents During the Juno Mission. Journal of Geophysical Research:
572 Space Physics 127, e2021JA030040. https://doi.org/10.1029/2021JA030040

573 Nichols, J.D., Yeoman, T.K., Bunce, E.J., Chowdhury, M.N., Cowley, S.W.H., Robinson, T.R.,
574 2017b. Periodic Emission Within Jupiter's Main Auroral Oval. Geophysical Research Letters
575 44, 9192–9198. https://doi.org/10.1002/2017GL074824

576 Pan, D.-X., Yao, Z.-H., Manners, H., Dunn, W., Bonfond, B., Grodent, D., Zhang, B.-Z., Guo, R.-
577 L., Wei, Y., 2021. Ultralow-Frequency Waves in Driving Jovian Aurorae Revealed by
578 Observations From HST and Juno. Geophysical Research Letters 48, e2020GL091579.
579 https://doi.org/10.1029/2020GL091579

580 Radioti, A., Gérard, J.-C., Grodent, D., Bonfond, B., Krupp, N., Woch, J., 2008. Discontinuity in
581 Jupiter's main auroral oval. Journal of Geophysical Research: Space Physics 113.
582 https://doi.org/10.1029/2007JA012610

583 Ray, L.C., Achilleos, N.A., Vogt, M.F., Yates, J.N., 2014. Local time variations in Jupiter's
584 magnetosphere-ionosphere coupling system. Journal of Geophysical Research: Space
585 Physics 119, 4740–4751. https://doi.org/10.1002/2014JA019941

586 Saur, J., Janser, S., Schreiner, A., Clark, G., Mauk, B.H., Kollmann, P., Ebert, R.W., Allegrini, F.,
587 Szalay, J.R., Kotsiaros, S., 2018. Wave-Particle Interaction of Alfvén Waves in Jupiter's
588 Magnetosphere: Auroral and Magnetospheric Particle Acceleration. Journal of Geophysical
589 Research: Space Physics 123, 9560–9573. https://doi.org/10.1029/2018JA025948

590 Sulaiman, A.H., Mauk, B.H., Szalay, J.R., Allegrini, F., Clark, G., Gladstone, G.R., Kotsiaros, S.,
591 Kurth, W.S., Bagenal, F., Bonfond, B., Connerney, J.E.P., Ebert, R.W., Elliott, S.S., Gershman,
592 D.J., Hospodarsky, G.B., Hue, V., Lysak, R.L., Masters, A., Santolík, O., Saur, J., Bolton, S.J.,

2022. Jupiter's Low-Altitude Auroral Zones: Fields, Particles, Plasma Waves, and Density Depletions. Journal of Geophysical Research: Space Physics 127, e2022JA030334. https://doi.org/10.1029/2022JA030334

Tao, C., Sahraoui, F., Fontaine, D., de Patoul, J., Chust, T., Kasahara, S., Retinò, A., 2015. Properties of Jupiter's magnetospheric turbulence observed by the Galileo spacecraft. Journal of Geophysical Research: Space Physics 120, 2477–2493. https://doi.org/10.1002/2014JA020749

Vogt, M.F., Kivelson, M.G., Khurana, K.K., Walker, R.J., Bonfond, B., Grodent, D., Radioti, A., 2011. Improved mapping of Jupiter's auroral features to magnetospheric sources. Journal of Geophysical Research: Space Physics 116. https://doi.org/10.1029/2010JA016148

Yao, Z.H., Bonfond, B., Grodent, D., Chané, E., Dunn, W.R., Kurth, W.S., Connerney, J.E.P., Nichols, J.D., Palmaerts, B., Guo, R.L., Hospodarsky, G.B., Mauk, B.H., Kimura, T., Bolton, S.J., 2022. On the Relation Between Auroral Morphologies and Compression Conditions of Jupiter's Magnetopause: Observations From Juno and the Hubble Space Telescope. Journal of Geophysical Research: Space Physics 127, e2021JA029894. https://doi.org/10.1029/2021JA029894

Yung, Y.L., Gladstone, G.R., Chang, K.M., Ajello, J.M., Srivastava, S.K., 1982. H2 fluorescence spectrum from 1200 to 1700 A by electron impact - Laboratory study and application to Jovian aurora. The Astrophysical Journal 254, L65–L69. https://doi.org/10.1086/183757